Deposition And Characterization of Seed Layers for Zno Nanostructures: A Comparative Study of Metal and Metal Oxide Thin Films

Pooja Yadav, Research Scholar, Dept. of Science, SunRise University, Alwar (Rajasthan)
Dr. Rajkumar Maurya, Associate Professor, Dept. of Science, SunRise University, Alwar (Rajasthan)

Abstract

In this study, we take a look at how seed layer thin films affect the wettability, optical, structural, microstructural, and sensing characteristics of ZnO nanostructures made by hydrothermal techniques. For the purpose of growing nanostructures, two seed layer types are studied: metal and metal oxides. Metals analysed include Indium (In), Tin (Sn), and Gold (Au), while oxides of these metals include zinc oxide (ZnO), thermally oxidised Indium and Tin, and Gold. Using thermal evaporation processes, all thin films are deposited. Unlike ZnO thin films, which require the matching oxide source, metal thin films are made by evaporating the metals themselves. The metal films of indium and tin oxide are heated and then oxidised in an air atmosphere to form the oxide films. In order to create the groundwork for future paper that delve into the growth and characteristics of ZnO nanostructures, this paper describes the processing parameters and structural features of the seed layer films.

Keywords: **Hydrothermal synthesis, Nanostructures, Seed layers, Zinc Oxide (ZnO), Wettability properties.**

1.1 Introduction

One of the goals of this work is to investigate the seed layers' function in controlling the ZnO nanostructures' growth patterns after hydrothermal synthesis, as mentioned in the introductory chapter. This chapter begins by discussing the seed layers' structure and features. Indium, tin, and gold, as well as indium, tin, and zinc oxides, make up the seed layers. The films of ZnO are made by first evaporating the ZnO and then thermally annealing them in air to attain stoichiometry; in the case of In and Sn oxides, this process involves annealing the corresponding metal films in air. The films are examined using optical techniques, scanning electron microscopy, and x-ray diffraction.

1.1.1 Organisation and microstructure Thin films of ZnO: The X-ray diffraction (XRD) patterns of the films as-deposited, captured at two separate sites, are displayed in figures 1.1(a) and (b). As insets, you can see the matching FESEM images. The films that were deposited were found to be a mixture of zinc and zinc oxide. Two peaks, one for the (0 0 2) plane of Zn metal and the other for the (0 0 1) plane of wurtzite ZnO, are identified. Figure 1.1(a) shows flat, homogeneous surface morphology with spherical particles 50–70 nm in diameter, while Figure 1.1(b) shows densely packed spherical particles 40–50 nm in diameter, with smaller particles 10–30 nm in diameter superimposed on top.
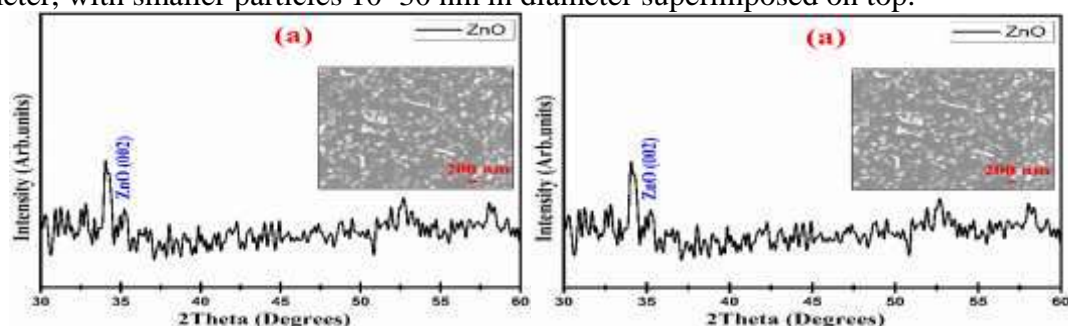

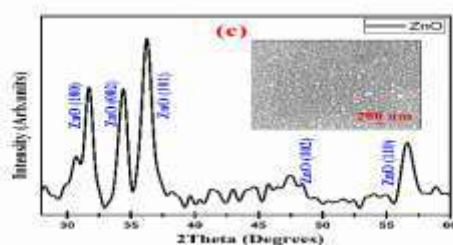**Fig. 1.1: XRD patterns and FE-SEM images of ZnO seed layers (a) and (b) as-deposited**

Fig. 1.1: XRD patterns and FE-SEM images of ZnO seed layers (c) annealed at 400 °C

for 2 hours.

The films were oxidised to perfection by annealing them at 400 °C for 2 hours because they were a mixture of metal and metal oxide. Following annealing, the XRD pattern shown in figure 1.1 (c) only reveals diffraction peaks corresponding to the (100), (002), (101), (102), and (110) planes of wurtzite ZnO; peaks linked to metallic Zn vanish. The ZnO crystal structure with a hexagonal wurtzite index is used in all diffraction peaks (JCPDS file no: 80-0074). Particles of ZnO with a diameter ranging from 30 to 50 nanometres are more uniformly distributed across the surface. Zinc oxide's crystal structure is not orientated in a particular way. All subsequent investigations relied on this optimised approach to produce stoichiometric ZnO. Next, we will show how the structure and microstructure are affected by seed layers of varying thicknesses (100-400 nm) deposited by thermal evaporation in a high vacuum. Images 1.2–1.5 display the surface microstructure of ZnO thin films with thicknesses of 100 nm, 150 nm, 200 nm, and 400 nm, respectively. Densely packed spherical particles of dimension 30-50 nm make up the microstructure of the 100 nm thick ZnO at different magnifications depicted in Figure 1.2 (a-c).
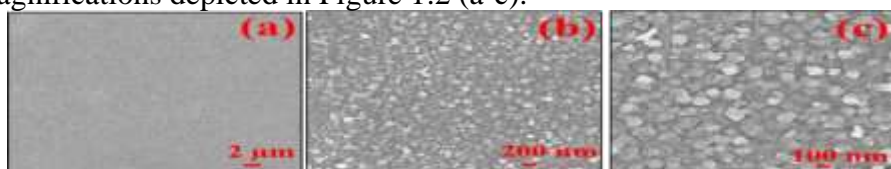

Fig. 1.2 (a-c): FE-SEM images of 100 nm ZnO thin film at different magnifications

Sharpening the edges of the spherical particles to 150 nm thickness produces a variety of non-spherical morphologies (figure 1.3(a-c)).

Fig. 1.3 (a-c): FE-SEM images of 150 nm ZnO thin film at different magnifications

The particles have mostly rectangular forms, with just a small percentage being longitudinally elongated. These microstructures are three-dimensional (3D) because the particles' elongation caused them to extend beyond the surface of the plane. This three-dimensional configuration causes surfaces to develop voids on the order of microns. By raising the film thickness to 200 nm, these particles undergo a transformation into giant spherical particles of 200 nm in size (figure 1.4(a-c)).
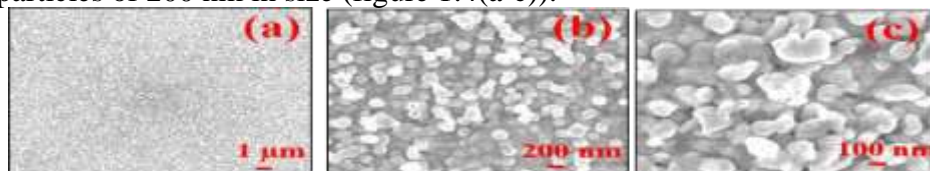

Fig. 1.4 (a-c): FE-SEM images of 200 nm ZnO thin film at different magnifications

The presence of empty spaces between the particles indicates that their packing density has decreased. The microstructure of the 400 nm layer is completely different. The surface is made up of vertically orientated twisted flakes that are 30-50 nm long and 400-500 nm wide (figure 1.5(a-c)).
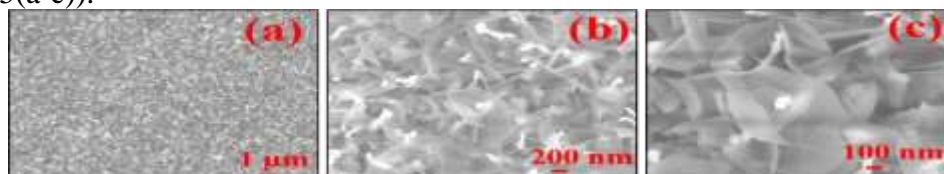

Fig. 1.5 (a-c): FE-SEM images of 400 nm ZnO thin film at different magnifications

There has been a dramatic shift in the evolution of surface microstructures and packing density as a result of the thickening of the ZnO film. It is impossible to ignore the role that surface roughness played in the development of nanowires. The surface microstructure and roughness of the ZnO films appear to be affected by thickness variation. Aside from this, nanowires with smaller dimensions may result from grains with smaller sizes. As shown in

Figure 1.6(a-d), the XRD-examined thin films' phase development and crystallographic data are displayed. The ZnO crystal structure with a hexagonal wurtzite index is used in all diffraction peaks (JCPDS file no: 80-0074). This finding provides more evidence that the microstructure has changed due to variations in ZnO thin film thickness, but the films have maintained their structural purity. No signs of unreacted metallic Zn have been detected. The (100), (002), (101) and (110) planes of the hexagonal wurtzite phase of ZnO are indexed to the conspicuous diffraction peaks at 2θ=31.64, 34.12, 36.2, and 56.6 degrees, respectively.
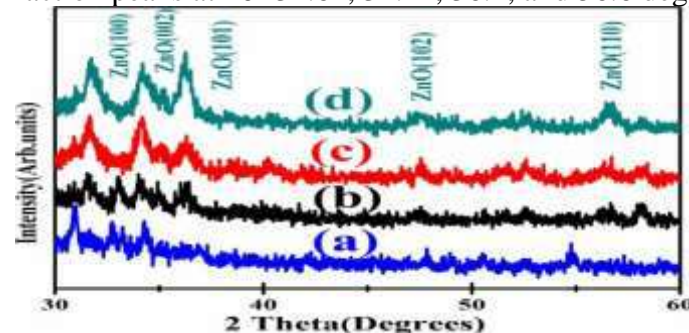

Fig. 1.6: X-ray diffraction patterns of ZnO seed layers of (a) 100 nm, (b) 150 nm, (c) 200 and (d) 400 nm thickness respectively

The 100 nm samples' extremely diffuse peaks are caused by the nano-crystalline sheets. The relative intensities of the several ZnO peaks have diminished slightly, suggesting a shift in the film's preferred orientation. The (101) peak's relative strength decreases in the 200 nm film, but the (110) plane's peak intensity increases in the 400 nm film. Importantly, the films are stoichiometric ZnO (within XRD detection limits), since no peaks associated with metallic Zn are present. After being created by thermal evaporation from a Zn or ZnO source, ZnO thin films must undergo post-deposition heat treatment in order to crystallise, as is well known. According to Scherrer's formula, the films in this situation are similarly nano-crystalline, with crystallite sizes ranging from 20-25 nm. Further, as the thickness increases, the peak positions move to higher 2θ values, suggesting that the residual stresses within the ZnO films change at different thicknesses. The discrepancy between the glass substrate's thermal expansion coefficient and that of the ZnO is probably the source of these residual stresses. This discrepancy was ascribed by Liu et al. to surface effects, which lead to lattice deformations and a decrease in the lattice parameter. For the same reason, this may explain why microstructures vary with thickness. Because of its nano-crystalline nature, densely packed spherical nanostructures, and relatively smooth surface, the 100 nm ZnO film stands out. It was deduced that the 100 nm ZnO film would be the best material to use for creating 1D nanostructural entities with vertically aligned ZnO layers based on the aforementioned findings and literature.

1.1.2. The optical characteristics of ZnO seed layers, including photoluminescence and Raman spectroscopy

To find flaws in the ZnO films, strong probes like photoluminescence and Raman spectroscopy can be used. Figure 1.7(a) shows that the PL spectra of the ZnO seed layers of varying thickness exhibit a clearly visible peak at approximately 550 nm and a somewhat less intense peak at about 380 nm. The near band-edge (NBE) PL peak at about 380 nm and the defect associated peak at around 550 nm of ZnO have been extensively studied and reported. In contrast to the UV-NBE, which is thought to be caused by the transition from the n=1 state to the exciton continuum state (P-line) by exciton-exciton scattering, the emission around 550 nm is typically linked to oxygen vacancies (Vo"). Compared to the emission in the visible area, the UV-NBE is noticeably weaker here. This would indicate that the films include a significant amount of oxygen vacancies or Zn interstitials, which are defects. An other intriguing feature is that as the thickness increases, the UV-NBE intensity increases but the defect-related peak intensity decreases. A redshift in both peak positions is also present during this occurrence. Burstein-Moss band filling effect or band gap shrinking via charge transfer from unreacted Zn to ZnO have been proposed as explanations for the red-shift of the band edge emission.
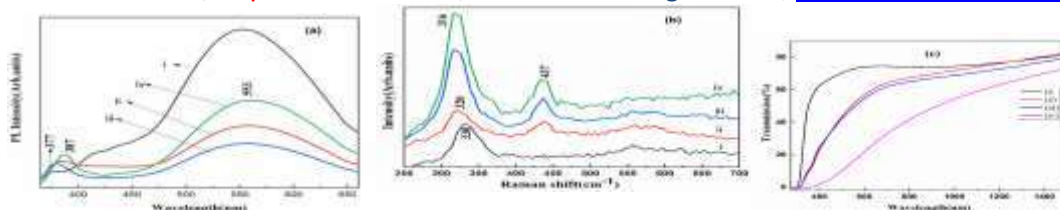
Fig. 1.7: Effect of thickness of ZnO films on the (a) photoluminescence, (b) Raman spectra, (c)Optical spectra i=100 nm; ii=150 nm; iii=200 nm; iv=400 nm.

Figure 1.7(b) shows the Raman spectra of the films, which back up these findings. At 330 cm^{-1}, there is a prominent Raman band that becomes stronger as the thickness increases and blue-shifts to 316 cm^{-1}. For a layer with a thickness of 100 nm, the strongest Raman band of ZnO, which is typically located at 437 cm^{-1}, is barely discernible. The peak becomes more noticeable for films of 400 nm thickness and grows in intensity as film thickness increases. With increasing film thickness, the ratio of high wavenumber to low wavenumber peaks becomes stronger. Previous work has shown that the low wavenumber peak at 330 cm^{-1} is a second-order Raman scattering peak caused by multi-phonon scattering processes. The reason for this is that, like GaN, ZnO has an E2 (high) - E2 (low) mode that is associated with the phonons at the zone boundary. The bulk of the studies on this low wavenumber peak have occurred in metal-doped ZnO, hence the appearance of these modes in un-doped ZnO thin films is unique. As an example, it is evident that the peak intensity increases with increasing dopant concentration in Mn doped ZnO. When there is disorder in the material, like flaws or vacancies, it permits phonons with different symmetries to scatter and have their peak intensified, a phenomenon known as multi-phonon processes. Heat treatment causes an increase in strain at the film-substrate interface, which is responsible for the peak's blueshift. The results of the PL and Raman spectroscopy show that the thin coatings that held the nanowire arrays together had flaws. Figure 1.7 (c) shows the optical transmission spectra, which show that the ZnO seed layers have a transmission of 60% to 80% between 300 and 1500 nm. As the seed layer thickness lowers, the transmission of ZnO nanostructures rises. As the thickness increases, the band gap falls from 3.9 eV to 3.4 eV. A strong absorption peak and distinct absorption shoulder are visible in the transmission spectra of the various ZnO seed layer thicknesses in the ultraviolet (UV) range of 300–400 nm. The ZnO nanostructures' quantum confinement effect is to blame for this. The results of these investigations demonstrate that ZnO thin films exhibit a high defect density at thinner layers, which diminishes with increasing thickness. These flaws originated in the thermal evaporation method, which is used to prepare thin films. The formed coatings create non-stoichiometry when high melting point minerals, as ZnO, undergo thermal evaporation. As seen in the previously displayed PL and Raman spectra, heat treatment is an attempt to decrease flaws; this is somewhat effective. The investigation of HP of ZnO nanostructures is being conducted on a film with a 100 nm thickness because the surface contains densely packed nanoparticles of the lowest size. On the other hand, PL and Raman spectra show that the film surfaces have a significant density of flaws.

1.2. Seed layers of indium (In) and tin (Sn) and their microstructure : How the ZnO structures developed on top of the seed layers develop is heavily influenced by the shape of the seed layers themselves. Figure 1.8(a-c) shows that the surface of the as-deposited In (InA) film, which is 10 nm thick, contains larger agglomerates with a diameter of 100 nm, layered with smaller particles with a diameter of 10–20 nm. A more consistent shape, with particles 30 nm in size, is achieved by annealing the In seed layers (InO) at 200°C for 2 hours (figure 1.8(d-f)).
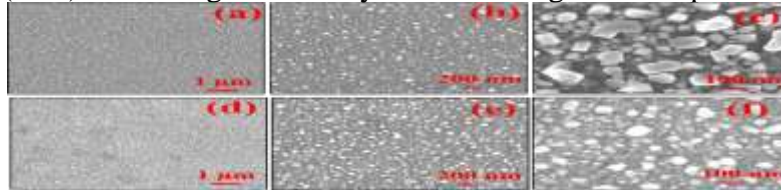

Fig. 1.8: FE-SEM images of the top surface of the 10 nm InA film (a-c), InO film (d-f) at different magnifications

The as-deposited films (SnA) containing Sn seed layers exhibit big cuboidal particles (Figure 1.9(a-c)). The particles were broken up into spherical agglomerates of 30-50 nm in size after annealing the Sn seed layers (SnO) at 300°C for 2 hours (figure 1.9(d-f)).Large agglomerates with a diameter of 80-100 nm are superimposed on smaller particles with a diameter of 10-20 nm on the surface of the 20 nm thick InA film (figure 1.10 (a-c)). Figure 1.10 (d-f) shows that after annealing the In seed layers (InO) at 200°C for 2 hours, the morphology becomes more homogeneous, with particles measuring 20-30 nm in size. Figure 1.11(a-c) shows that as-deposited films (SnA) containing Sn seed layers include big cuboidal particles.

Fig. 1.9: FE-SEM images of the top surface of the 10 nm SnA film (a-c), SnO film (d-f) atdifferent magnifications

Figure 1.11(d-f) shows that after annealing the Sn seed layers (SnO) at 300°C for 2 hours, the particles were broken up into spherical agglomerates with a size range of 30-50 nm.
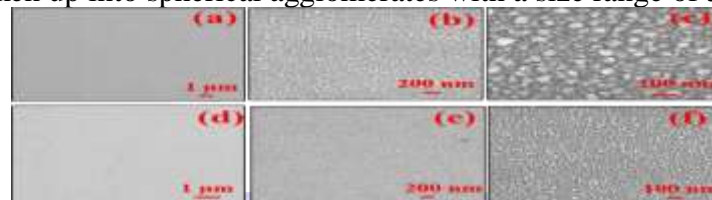

Fig. 1.10: FE-SEM images of the top surface of the 20 nm InA film (a-c), InO film (d-f) atdifferent magnifications
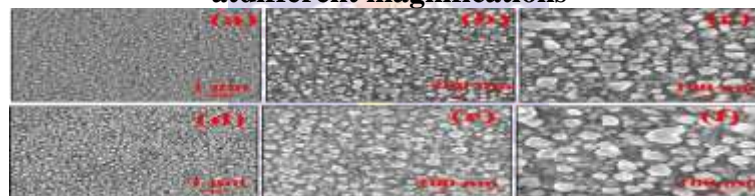

Fig. 1.11: FE-SEM images of the top surface of the 20 nmSnA film (a-c), SnO film (d-f) atdifferent magnifications

Large agglomerates with a diameter of 80-100 nm are superimposed on smaller particles with a diameter of 10-20 nm on the surface of the 30 nm thick seed layer (figure1.12(a-c)). Particles with a size range of 10–20 nanometres are the end product of annealing the In seed layers (InO) at 200 degrees Celsius for two hours (Figure 1.12(d–f)).
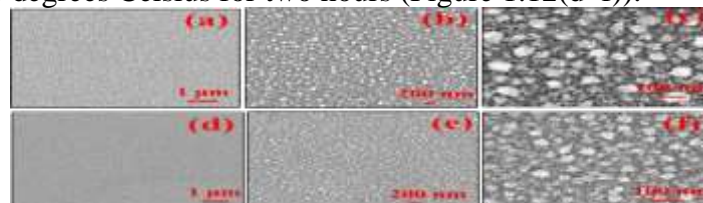

Fig. 1.12: FE-SEM images of the top surface of the 30 nm InA film (a-c), InO film (d-f) atdifferent magnifications

Figure 1.13(a-c) shows that the as-deposited films (SnA) of Sn seed layers have big cuboidal particles measuring 100 nm in size, with smaller particles measuring 30-50 nm in diameter superimposed on top. The particles were broken up into spherical agglomerates of around 20-30 nm in size after annealing the Sn seed layers (SnO) at 300°C for 2 hours (figure 1.13(d-f)).
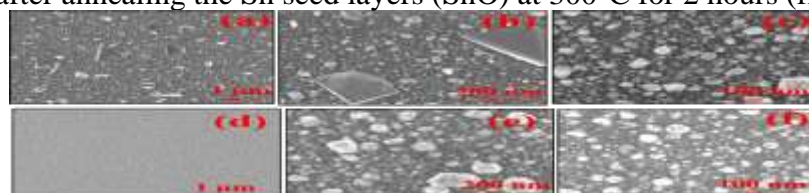

Fig. 1.13: FE-SEM images of the top surface of the 30 nm SnA film (a-c), SnO film (d-f) atdifferent magnifications

Figure 1.14(a-c) illustrates that the surface of the 40 nm thick seed layer displays massive agglomerates with a diameter of 100-120 nm above smaller particles with a diameter of 20-30 nm. A more consistent shape, with particles 80-100 nm in size, is achieved by annealing the In seed layers (InO) at 200ºC for 2 hours (figure 1.14(d-f)).
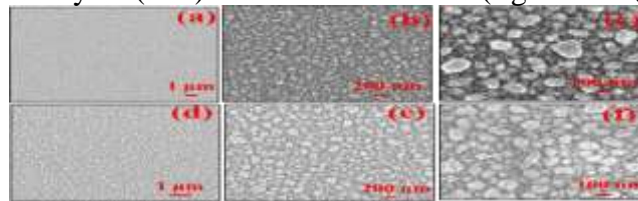

Fig. 1.14: FE-SEM images of the top surface of the 40 nm InA film (a-c), InO film(d-f) at different magnifications

Particles of 30–50 nm in diameter are superimposed on top of larger cuboidal ones with a size of 100–150 nm in the as-deposited films (SnA) of Sn seed layers (figure 1.15(a-c)). These particles with a diameter of 100 nm were broken up and superimposed spherical agglomerates of 20-30 nm were formed after annealing the Sn seed layers (SnO) at 300ºC for 2 hours (figure 1.15(d-f)).
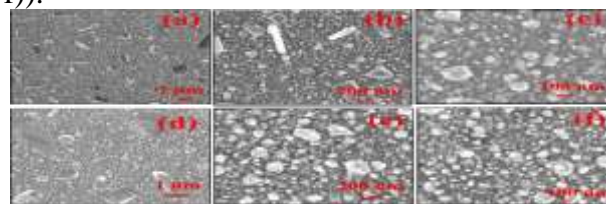

Fig. 1.15: FE-SEM images of the top surface of the 40 nm SnA film (a-c), SnO film (d-f) atdifferent magnifications

The situation is similar when the seed layer thickness is 50 nm, as seen in figure 1.16(a-c): big agglomerates with a diameter of 120-150 nm are layered with smaller particles with a diameter of 20-30 nm. A more consistent shape, with larger particles of 80–100 nm superimposed on smaller ones of 20–30 nm, is achieved by annealing the in seed layers (InO) at 200ºC for 2 hours (figure 1.16(d-f)). Figure 1.17(a-c) shows that the as-deposited films (SnA) of Sn seed layers have big cuboidal particles measuring 200-300 nm in size, with smaller particles measuring 60-80 nm in diameter superimposed on top. Figure 1.17(d-f) shows that after annealing the Sn seed layers (SnO) at 300ºC for 2 hours, the particles were broken up into spherical agglomerates with a size range of 30-50 nm. The crystallographic data and phase development of the In and Sn seed layers studied by XRD are shown in figure 1.18 ((a)-(b)). Size of crystallites in InA seed layers is 40 nm, while in InO seed layers it is 32 nm.
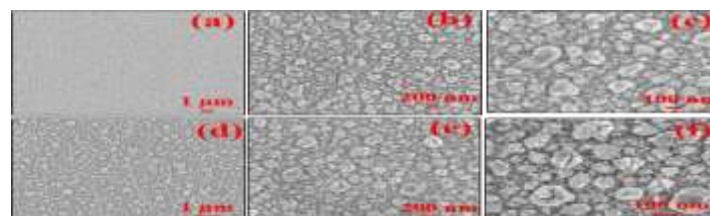

Fig. 1.16: FE-SEM images of the top surface of the 50 nm InA film (a-c), InO film (d-f) atdifferent magnifications

Likewise, SnA and SnO both have crystallite sizes of about 60 nm and 41 nm, respectively. The fact that the strain was tensile across all seed layers was the most intriguing finding
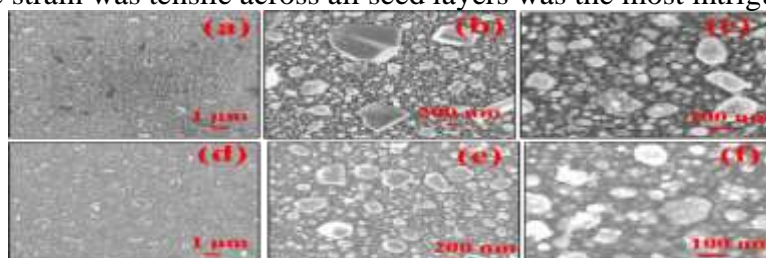

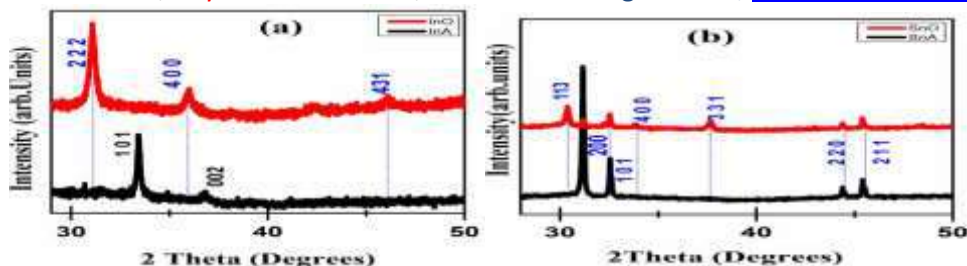**Fig. 1.17: FE-SEM images of the top surface of the 50 nm SnA film (a-c), SnO film (d-f) atdifferent magnifications**

Fig. 1.18: X-ray diffraction patterns of (a) InA and InO, (b) SnA and SnO seed layers

Lattice parameters for In crystallise at a=b=3.25Å, c=4.94 Å, and for Sn it is a=b=5.83Å, c=3.18, respectively. This structure is centred around the body. The lattice parameters of rhombohedral Indium oxide are 5.48 Å, b=4.75 Å, and c=3.18 Å, but rutile tin oxide crystallises with different values. The significant lattice mismatch between the seed layers and ZnO is obviously the source of strain in the ZnO structures.

1.2.1. The InO and SnO seed layers' optical characteristics

Figure 1.19 (a) shows the optical transmission spectra, which show that the transmission increases by around 40% to 80% in the 300-1000 nm region as the thickness of the InO seed layers increases. As seed layer thickness decreases, indium oxidation transmission increases. As the thickness increases, the band gap falls from 3.8 eV to 3.6 eV. Figure 1.19 (b) shows that SnO seed layers exhibit very high transmission (between 30% and 80%) between 300 and 1000 nm. Less seed layer thickness results in higher SnO transmission. The band gap drops from 3.9 eV to 3.7 eV as a result of the thickening.
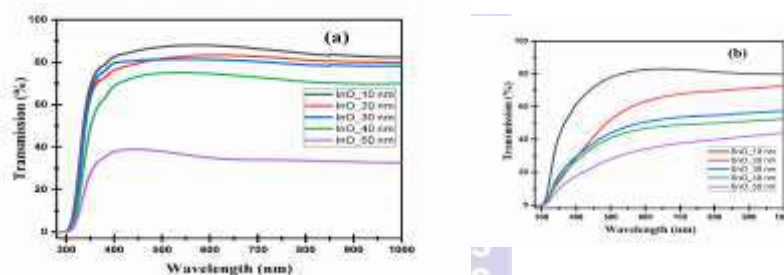

Fig. 1.19: Effect of seed layers thickness on transmission spectra of (a) InO and (b) SnO films. It is to be noted that the as-deposited InA and SnA films are metallic and, hence, do notshow any transmission.

1.3. The structure and microstructure of the seed layer of gold (Au)

Lastly, this study makes use of 100 nm thick Au thin films created by thermal evaporation as the seed layer. Particles with a diameter of 10–20 nm are packed densely into the spherical surface microstructure seen in Figure 1.20 (a-b).
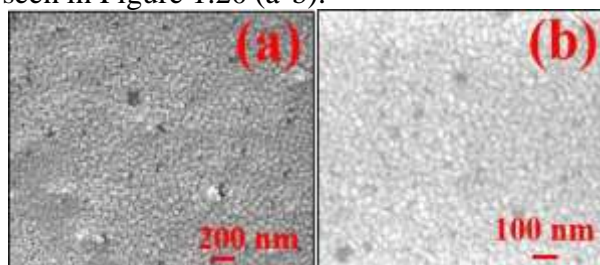

Fig. 1.20 (a-b): FE-SEM image of the top surface of the 100 nm Au seed layer at differentmagnification
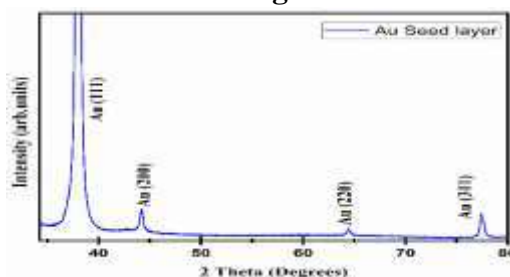

Fig. 1.21: X-ray diffraction pattern of the Au seed layer

1.3.1 Physical characteristics of the seed layer made of gold (Au)

Localised Surface Plasmon Resonance (LSPR) causes an absorption peak at 520 nm, as shown in Figure 1.22 of the optical transmission spectra. The presence of the LSPR peak suggests that the Au films are nano-crystalline.
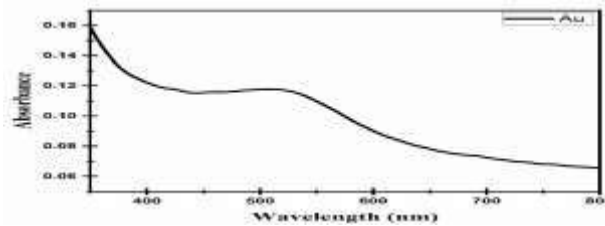

Fig. 1.22: Optical absorption spectrum of the Au seed layer

Conclusion

To summarise, film samples of In, Sn, and Au metals as well as thin films of In_2O_3, SnO, and ZnO were produced on glass substrates using thermal evaporation in a vacuum. Their effectiveness as seed layers for the formation of ZnO nanostructures was evaluated. The oxides were produced by optimising a thermal oxidation process. It was found that ZnO seed layer thin films of 100 nm thickness are ideal for growing nanostructures, taking into account the surface microstructure, nature of flaws and vacancies, and nanocrystalline nature. It would appear that the structures and microstructures necessary for the formation of ZnO nanostructures are present in the 10 nm thick films of In and Sn metals. In order to facilitate the formation of ZnO nanostructures, the relevant oxides are further refined for use as seed layer thin films. Our 100 nm thick gold thin film is now ready to be used as a seed layer.

Acknowledgment

References

1. Zhao, B., Wang, L., Li, X., & Zhao, D. (2016). Seed Layer Effects on ZnO Nanowire Growth and Device Performance. *Journal of Materials Science*, 51(8), 3950-3958.
2. Singh, A., Sharma, R., & Gupta, N. (2018). Influence of Seed Layer on the Structural and Optical Properties of Hydrothermally Synthesized ZnO Nanorods. *Materials Chemistry and Physics*, 211, 344-350.
3. Wang, C., Wu, X., & Li, Y. (2017). Deposition of Indium Tin Oxide Seed Layers for Enhanced ZnO Nanostructure Growth. *Thin Solid Films*, 629, 1-8.
4. Kumar, P., & Singh, M. (2015). Thermally Evaporated Au and ZnO Seed Layers for ZnO Nanostructure Growth. *Journal of Nanoparticle Research*, 17(5), 245.
5. Liu, J., Zhang, Y., & Chen, G. (2019). Optical and Structural Properties of ZnO Nanostructures Grown on Various Seed Layers. *Journal of Applied Physics*, 125(16), 164302.
6. Gupta, R., Kumar, A., & Chatterjee, S. (2020). Role of Seed Layer Composition on the Morphology and Sensing Properties of ZnO Nanowires. *Sensors and Actuators B: Chemical*, 304, 127387.
7. Kaur, J., & Mehra, R. M. (2017). Effect of Seed Layer Thickness on the Growth of ZnO Nanorods by Hydrothermal Method. *Materials Science in Semiconductor Processing*, 69, 26-32.
8. Ahmed, M., & Khan, Z. R. (2016). Investigation of Microstructural and Wettability Properties of ZnO Nanostructures Grown on Metal and Metal Oxide Seed Layers. *Applied Surface Science*, 371, 237-244.
9. Das, S., Nanda, K. K., & Raychaudhuri, A. K. (2015). Influence of Different Seed Layers on the Growth and Optical Properties of ZnO Nanostructures. *Journal of Physics D: Applied Physics*, 48(35), 355301.
10. Srivastava, P., & Kumar, V. (2018). Correlation Between Seed Layer Properties and ZnO Nanorod Growth. *Materials Letters*, 223, 123-126.
11. Chaudhary, S., & Verma, K. (2019). Deposition Techniques for Metal and Metal Oxide Seed Layers and Their Impact on ZnO Nanostructure Properties. *Surface and Coatings Technology*, 357, 398-406.
12. Bhattacharya, P., & Pal, A. K. (2016). Seed Layer-Dependent Hydrothermal Growth of ZnO Nanostructures: Structural, Optical and Sensing Properties. *Journal of Alloys and Compounds*, 665, 233-241.